The Journal of Chemical Physics ARTICLE scitation.org/journal/jcp

Ozone destruction due to the recombination of oxygen atoms

Cite as: J. Chem. Phys. 155, 164307 (2021); doi: 10.1063/5.0064361
Submitted: 22 July 2021 • Accepted: 11 October 2021 •
Published Online: 28 October 2021

Andrey A. Pershin,[1,2] Aleksei P. Torbin,[1] Paul A. Mikheyev,[1] Ralf I. Kaiser,[1,3] Alexander M. Mebel,[2,4,a)] and Valeriy N. Azyazov[1,2]

AFFILIATIONS

[1] Lebedev Physical Institute, Samara 443011, Russia
[2] Samara National Research University, Samara 443086, Russia
[3] Department of Chemistry, University of Hawaii at Manoa, Honolulu, Hawaii 96822, USA
[4] Department of Chemistry and Biochemistry, Florida International University, Miami, Florida 33199, USA

[a)] Author to whom correspondence should be addressed: mebela@fiu.edu

ABSTRACT

Kinetics of ozone destruction due to the recombination of oxygen atoms produced by pulsed 266 nm laser photolysis of O_3/M (M = CO_2 and/or N_2) mixtures was studied using the absorption and emission spectroscopy to follow time evolutions of O_3 and electronically excited molecules O_2^* formed in the recombination process $2O(^3P) + M \rightarrow O_2^* + M$. An unexpected high ozone destruction rate was observed when O_2^* was present in the system. The kinetic model developed for the oxygen nightglow on the terrestrial planets was adapted to interpret the detected temporal profiles of the ozone number density and the O_2^* emission intensities. It was deduced that the vibrationally excited singlet delta oxygen molecule $O_2(a^1\Delta, v)$ formed in the secondary processes reacts efficiently with ozone in the process $O_2(a^1\Delta, v \geq 3) + O_3 \rightarrow 2O_2 + O$, and the rate constant of this process was estimated to be 3×10^{-11} cm^3 s^{-1}. *Ab initio* calculations at the CASPT2(14, 12)/cc-pVTZ/UωB97XD/cc-pVTZ level of theory were applied to find the reaction pathway from the reactants to products on the O_5 potential energy surface. These calculations revealed that the $O_2(a^1\Delta) + O_3$ reaction is likely to proceed via singlet–triplet intersystem crossing exhibiting an energy barrier of 9.6 kcal/mol, which lies between two and three quanta of vibrational excitation of $O_2(a^1\Delta)$, and hence, $O_2(a^1\Delta, v)$ with $v \geq 3$ could rapidly react with ozone.

I. INTRODUCTION

Atmospheric oxygen is both the basis of life and its protection from the UV solar radiation. UV light fragments oxygen (O_2) and ozone (O_3) molecules to form oxygen atoms, which then recombine to form excited oxygen molecules. The latter manifest themselves in the emission of light in a wide range of the spectrum in the glow of not only the atmosphere of the Earth but also of Mars,[1] Venus,[2] and exoplanets such as HD 189733b containing oxygen in their atmospheres.[3–5] In addition, excited molecular oxygen formed via recombination of atomic oxygen is involved in energy exchange and chemical processes, thus significantly affecting the atmospheric kinetics and molecular concentration profiles depending on the altitude. One of the key atmospheric three-body recombination processes, process 1 (Table I), produces an oxygen molecule O_2^* in one of the seven electronic states[6,7]—$X^3\Sigma_g^-$, $a^1\Delta_g$, $b^1\Sigma_g^+$, $c^1\Sigma_u^-$, $A'^3\Delta_u$, $A^3\Sigma_u^+$, or $^5\Pi_g$. In the following, these states are designated as X, a, b, c, A', A, and Π, respectively. Three of them, c, A', and A, are usually called Herzberg states. In the following, they are denoted as O_2^H. These excited oxygen molecules play an important role in the radiative and collisional kinetics of terrestrial atmospheres.[6–15] O_2^* is a prominent emitter in the terrestrial atmospheres, and the strongest emission lines in the night airglow[1,16–18] are represented by the following transitions: IR atmospheric system $O_2(a \rightarrow X)$, atmospheric system $O_2(b \rightarrow X)$, and Herzberg I system $O_2(A \rightarrow X)$.

A large number of studies on spectroscopy and kinetics of oxygen were described in the comprehensive reviews by Slanger and Copeland[6] and Huestis.[7] In particular, the following information found in these reviews is relevant to the current work. The yields of O_2 in the electronic states X, a, b, c, A', A, and Π produced in process 1 were calculated[25,26] to be 0.09, 0.05, 0.02, 0.03, 0.16, 0.06, and 0.59 at T = 300 K, respectively. Reaction 1 populates mostly the

TABLE I. Reactions and rate constants used in the analysis of the O_3/M photolysis system.

No.	Reaction	Rate constant, T = 300 K ($cm^3\ s^{-1}$)	References
1	$O(^3P) + O(^3P) + M \rightarrow O_2^* + M$	$k_1^{N_2} = 3 \times 10^{-33}\ cm^6\ s^{-1}$ $k_1^{CO_2} = 2.5 \times k_1^{N_2}$	19 1
1a	$O(^3P) + O(^3P) + M \rightarrow O_2^H + M$	$0.25 \times k_1^M$	(See text)
1b	$\rightarrow O_2(a,\ v) + M$	$0.75 \times k_1^M$	(See text)
2	$O_2^H + O(^3P) \rightarrow O_2(a,\ v) + O(^3P)$	1.3×10^{-11}	20
3	$O_2^H + O_2(a) \rightarrow O_2(a,\ v) + O_2$	8×10^{-11}	20
4	$O_2^H + M \rightarrow O_2 + M$	$k_4^{N_2} = 2 \times 10^{-13}$ $k_4^{CO_2} = 7 \times 10^{-13}$	(See text) 21
5	$O_2(a,\ v) + O(^3P) \rightarrow O_2(a,\ v-1) + O(^3P)$	$v \times k_{1\rightarrow0}^O$ $k_{1\rightarrow0}^O = 4 \times 10^{-13}$	22
6	$O_2(a,\ v) + M \rightarrow O_2(a,\ v-1) + M$	$v \times k_{1\rightarrow0}^M$ $k_{1\rightarrow0}^{N_2} = 3 \times 10^{-16}$ $k_{1\rightarrow0}^{CO_2} = 1.7 \times 10^{-14}$	(See text) 22 22 and 23
7	$O_3 + O_2(a,\ v \geq 3) \rightarrow O_2 + O_2 + O(^3P)$	$(3 \pm 1) \times 10^{-11}$	This work
8	$O_3 + O_2^H \rightarrow O_2(a,\ v) + O_2 + O(^3P)$	$(2 \pm 1) \times 10^{-10}$	This work
9	$O_3 + O_2(a) \rightarrow O_2 + O_2 + O(^3P)$	$5.2 \times 10^{-11} \exp(-2840/T)$	24
10	$O_3 + O(^3P) \rightarrow O_2 + O_2$	$2 \times 10^{-11} \exp(-2280/T)$	24

Π state of nascent O_2, although no one had been able to observe this state for a long time. The resonance-enhanced multiphoton ionization (REMPI) technique made it possible not only to detect $O_2(\Pi)$ but to also measure the rate constants of its collisional removal by CO_2, N_2, and O_2.[6] The total yield of nascent O_2 in Herzberg's states was about 25%[25,26] (process 1a). The collisional removal of the $O_2(A, v)$ molecule prepared in selected vibrational levels v has been studied by many authors,[27–30] while much less attention was paid to the other two Herzberg's states.[21,30,31] The quenching rate coefficients for $O_2^H(v)$ in collisions with CO_2, CO, N_2, and O_2 molecules were calculated using Landau–Zener and Rosen–Zener approximations.[32] Analysis of O_2^H (v) kinetics showed that these three states are collisionally coupled, and therefore, the input energy is distributed among them quickly.[6] The REMPI experiments[6,33] showed that collisions of O_2^H with CO_2, N_2, and O_2 molecules result in the formation of singlet oxygen molecules $O_2(b, a)$. $O_2(\Pi)$ is effectively quenched by N_2 and CO_2 with rate coefficients 1.7×10^{-11} and 4×10^{-11} $cm^3\ s^{-1}$, respectively; however, the final state is not established. Taking into account the fact that the observed $O_2(a\text{-}X)$ emission intensity approximately matches the total integrated rate of oxygen atom recombination of the Earth and Venus atmospheres,[7] it was concluded that the final excited electronic state is predominantly $O_2(a, v)$ (process 1b).

Extensive kinetic data are available on the processes involving the two lower excited states of oxygen $O_2(a, b)$, since they play key roles in atmospheric chemistry,[6,7,24,34] in oxygen-containing plasma,[35–37] and in the kinetics of the active medium of an oxygen–iodine laser.[38,39] Rate constants for $O_2(b)$ removal in collisions with O_2, N_2, CO_2, and H_2O have been recently measured over the temperature range from 297 to 800 K.[40] It has been reliably established that $O_2(b)$ is quenched by CO_2, N_2, O_2, H_2, C_2H_4, N_2O, H_2O, and CH_4 to $O_2(a)$ with a branching ratio close to unity.[41,42]

Pejaković and co-workers[22,43–46] reported the rate constants for collisional removal of vibrationally excited $O_2(b)$ and $O_2(a)$ by atmospherically relevant species. Recently,[23] rate constants for the vibrational relaxation of $O_2(a, v)$ by CO_2 have been measured for v = 1, 2, and 3. Kirillov[47,48] calculated the removal rates of singlet molecular oxygen $O_2(b, v$ = 0–15) in collisions with O_2, N_2, CO, and CO_2 molecules and $O_2(a, v$ = 0–15) in collisions with O_2 using the analytical expression based on the Rosen–Zener approximation.

There is little information about chemical reactions with oxygen in Herzberg states. It was suggested that O_2^H reacting with O_2 and N_2 produces ozone[49] and N_2O,[50] respectively. In contrast, there are extensive kinetic data on reactions involving the two lower excited states of oxygen $O_2(a, b)$.[6,7,24,34–38] The most important for atmospheric ozone chemistry are the reactions 9 from Table I and

$$O_2(b) + O_3 \rightarrow O_2 + O_2 + O(^3P).$$

The rate constant at 300 K for the reaction with $O_2(b)$ (1.0×10^{-11} $cm^3\ s^{-1}$) is four orders of magnitude higher than that for $O_2(a)$ (3.8×10^{-15} $cm^3\ s^{-1}$).[51] Both O_2^* appeared in reaction 1 and $O_2(b, a)$ formed in the energy-exchange processes are highly vibrationally excited. It was shown previously[34] that the vibrational energy stored in the ozone molecule accelerates the rate of reaction 9. In addition, it is reasonable to assume that vibrationally excited singlet oxygen $O_2(a, v)$ will react faster with the O_3 molecule (reaction 7).

Here, we report on the temporal profiles of the O_3 number density and the O_2^* emission intensities detected after photolysis of O_3/M mixtures. The obtained experimental data are analyzed based on the kinetic model for the oxygen nightglow on terrestrial planets proposed by Krasnopolsky[1] to reveal unexpected, rapid mechanisms of ozone destruction.

II. EXPERIMENTAL SECTION

Laser photolysis of ozone at 266 nm occurring in a gas mixture O_3/M produces oxygen atoms and vibrationally excited singlet oxygen molecule $O_2(a, v)$,

$$O_3 + h\nu_{266} \rightarrow O(^1D) + O_2(a, v) \rightarrow O(^3P) + O_2(X),$$

with the branching fraction for the first product channel of 90%.[24] $O_2(a, v)$ molecules have an initial population distribution of 0.57:0.24:0.12:0.07 over vibrational levels v = 0, 1, 2, and 3, respectively.[52] The fourth harmonic of a Nd:YAG laser (Solar Systems LQ829, pulse duration 10 ns, repetition rate 10 Hz) provided photolysis of O_3 at 266 nm in the photolysis cell, which have been described previously.[23,34] Laser radiation passed through the entrance and exit windows mounted on baffle arms (35 cm long) attached to the photolysis cell to reduce interference from scattered laser light. The laser beam was ~8 mm in diameter.

Gas velocity in the photolysis zone was typically 50–100 cm s^{-1}, which was fast enough to ensure that each pulse photolyzed a fresh sample of the gas mixture. Pressure in the photolysis cell was measured using a METRAN 100-DA sensor. Flow meters (Bronkhorst, MASS-VIEW MV-302, 304), Mass Flow Controllers (Alicat, MCS-5SLPM-D), and needle valves controlled gas flow rates. High purity gases O_2 (Linde, 99.9999%), CO_2 (Linde, 99.99%), and N_2 (Linde, 99.9999%) were used in the experiments. The cell was evacuated by an oil free scroll pump with the pumping rate adjusted by a needle valve. A laboratory ozonator (A-s-GOKSf-5-02-OZON) produced ozone from pure oxygen. Ozone was collected in a flask with silica gel (KSKG GOST 3956-76) immersed in a tank with cooled alcohol (−50/−100°C). Before the use, the flask was evacuated and purged with slow N_2 flow to remove the residual O_2 from the silica gel. On the course of experiments, a slow flow of N_2 eluted O_3. The initial ozone number density $[O_3]_{in}$, entering the photolysis zone, was monitored by absorption of 254 nm light from a low-pressure Hg lamp.

Emissions from the O_2 Herzberg's states were observed through a quartz window along the axis that was perpendicular to the photolysis laser beam. A 5 cm focal length lens collected the light and focused it on the entrance slit of a monochromator MDR-12 with a FWHM resolution of 40 nm. Time-resolved absorption spectroscopy at λ = 258 nm was employed to measure the O_3 number density in the photolysis zone. The detailed description of $[O_3]$ measurements is given elsewhere.[34,53] A continuous light-emitting diode (LED, UVTOP255) was used as a source of UV light for these measurements. A quartz lens (f = 1.5 cm) collected light from the LED and focused it into a quartz optical fiber that delivered it to the photolysis zone. A fraction of this light was collected by a second fiber that delivered it to a monochromator MDR-12 with a UV sensitive photomultiplier (PMT). Time resolved signals from the PMT were averaged and stored with the help of a digital oscilloscope (Agilent DSO1022A, 200 MHz bandwidth). The oscilloscope was triggered directly by the laser pulse.

III. RESULTS AND DISCUSSION

Typical time-resolved ozone number density $[O_3]$ profiles in the gas mixture $O_3/N_2(CO_2)$ photolyzed by E = 40 mJ/cm^2 laser pulses at a total gas pressure of P_{tot} = 780 Torr are presented in Fig. 1.

To maintain a constant total pressure, the partial pressures of CO_2 (P_{CO_2}) and N_2 (P_{N_2}) were varied with the constraint that $P_{N_2} + P_{CO_2} = P_{tot}$. Laser photolysis occurred at t = 0. The initial ozone number densities $[O_3]_{in}$ at t < 0 are also shown in Fig. 1. The negative time domain in the figures is a consequence of the absorption spectroscopy method and the oscilloscope triggering by the laser pulse. This allows the fraction of photolyzed ozone to be precisely controlled. Electronically excited oxygen atoms $O(^1D)$ produced in the photolysis are rapidly deactivated to the ground state $O(^3P)$ by collisions with both N_2 and CO_2. Thus, in all further discussions, the initial amount of $O(^3P)$ after photolysis was assumed equal to the number density of the photolyzed ozone $\Delta[O_3]_{ph} = [O]_0 = [O_3]_{in} - [O_3]_0$ (designations from Fig. 1). The terms in square brackets are number densities of the corresponding components.

Two main conclusions follow from the observed profiles in Fig. 1. First, fast ozone decomposition rate is observed for any mixture composition. The observed ozone removal cannot be interpreted using generally accepted models and published rate constants. According to them, the main channels of O_3 destruction are chemical reactions with singlet molecular oxygen $O_2(a)$ (process 9 in Table I) and atomic oxygen $O(^3P)$ (process 10). The dashed line in Fig. 1 represents the ozone temporal profile calculated with the help of this kinetic model under the conditions as for the lowest signal (P_{N_2} = 780 Torr and P_{CO_2} = 0 Torr). Second, addition of CO_2 inhibits the rate of ozone depletion and reduces the fraction of destroyed ozone $Z = \frac{[O_3]_0 - [O_3]_{inf}}{[O_3]_0}$ in the post-photolysis zone. The observed experimental data point at the need to elucidate other paths of ozone decomposition. The fast rate of ozone removal cannot be explained by an increase in the gas temperature, which is estimated by the formula

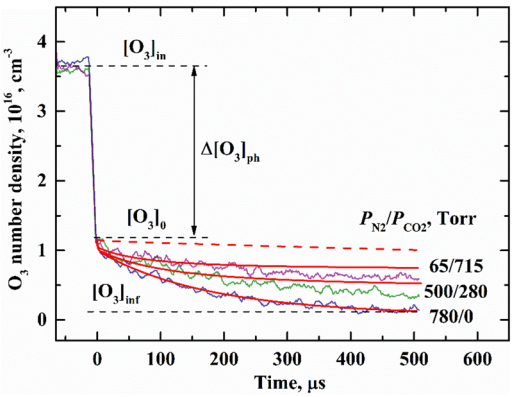

FIG. 1. Temporal profiles of the O_3 number densities for three mixtures of N_2/CO_2 buffer gases with constant total pressure $P_{N_2} + P_{CO_2}$ = 780 Torr, T = 300 K, $[O_3]_0$ = 1.1 × 10^{16} cm^{-3}, and $[O]_0$ = 2.6 × 10^{16} cm^{-3}. Smooth curves—$[O_3]$ profiles calculated using the model proposed in this study. Red dashed curve—$[O_3]$ decay profile resulting from the processes 9 and 10 under the conditions as for the lowest plot.

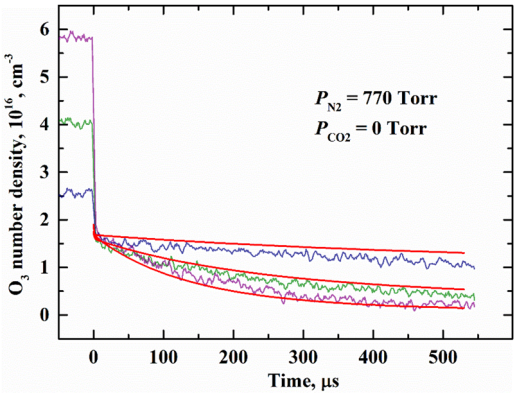

FIG. 2. Temporal profiles of the O_3 number densities at P_{N_2} = 770 Torr and T = 300 K for the same values of $[O_3]_0 = 1.9 \times 10^{16}$ cm^{-3} and different $[O_3]_{in}$. Smooth curves—profiles calculated using the model proposed in this study.

$$\Delta T = \frac{\Delta[O_3]_{ph}\left(E_{ph} - E_d - 0.9E_a\right)}{c_p},$$

where E_{ph}, E_d, and E_a are the energies of photolysis photon, ozone dissociation, and $O_2(a)$ excitation, respectively, and c_p is the heat capacity of the gas mixture. For the experimental conditions in Fig. 1, the temperature jump after photolysis is only about 10 K.

The composition of the gas mixture after the UV ozone photolysis (t = 0) includes the buffer gas M, remaining ozone O_3, oxygen atoms $O(^3P)$, and molecules $O_2(X)$, as well as singlet oxygen molecules in several vibrational states $O_2(a, v = 0–3)$. At our experimental conditions, the typical initial number densities are $[O_3]_0 \sim [O]_0 \sim [O_2(a)]_0 \sim 10^{16}$ cm^{-3}, $[M]/[O]_0 \sim 10^3$, and $[M]/[O_2(X)]_0 \sim 10^4$. Here and in the following, the subscript $_0$ denotes number densities at the moment right after the O_3 photolysis at t = 0. We neglected the processes involving $O_2(X)$ because its concentration in the mixture was insignificant. It was found[34] that the energy stored in vibrational modes of the O_3 molecule is involved in overcoming the activation barrier of reaction 9—with temperature dependence of the rate constant $k_9 = 5.2 \times 10^{-11} \exp(-2840/T)$ cm^3 s^{-1} for the ground state O_3.[51] For $v \geq 2$, the value of k_9 no longer depends on the internal vibrational energy. It is reasonable to assume that the $O_2(a, v)$ molecule will react faster with the ozone molecule (process 7) than $O_2(a)$ with equilibrium population of vibrational levels (process 9).

Figure 2 represents typical O_3 profiles after laser photolysis with N_2 buffer gas at 1 atm pressure when $[O_3]_0$ was held constant for three initial O_3 number densities. The required $[O_3]_0$ was achieved by adjusting the laser energy and $[O_3]_{in}$. Initial assessment of $[O_3]_{in}$ and laser energy was performed using the formulation of Beer's law proposed by Tellinghuisen and Phillips,[54] which takes into account the intensity and O_3number density gradients along the direction of the photolysis laser beam,

$$[O]_0 = \Delta[O_3]_{ph} = \frac{[O_3]_{in} \times \exp\left(\sigma\left([O_3]_{in} l - I_c\tau\right)\right)}{1 + \left(\exp\left(\sigma[O_3]_{in} l\right) - 1\right) \times \exp(-\sigma I_c \tau)},$$

where σ is the ozone absorption cross section at 266 nm, l is the absorption length, I_0 is the initial laser intensity, and τ is the laser pulse duration. The discrepancy between experimentally obtained and calculated values of $\Delta[O_3]_{ph}$ did not exceed 10%.

The fraction of destroyed ozone Z increases with the number density of photolyzed ozone $\Delta[O_3]_{ph}$. A similar phenomenon was observed in the N_2/CO_2 mixture (1/3, P_{tot} = 1 atm), with exception that the dependence of Z on $\Delta[O_3]_{ph}$ was weaker. Ozone temporal profiles for constant number densities $[O]_0$ and $[O_3]_0$ for three total pressures of N_2 (a) and CO_2 (b) are displayed in Fig. 3, which shows that a decrease in the buffer gas pressure leads to an increase in Z.

In this study, the kinetic model developed for the oxygen nightglow on terrestrial planets[1] was adapted to interpret the detected temporal profiles of the ozone number density and the O_2^* emission intensities. The reactions included in the model are collected in Table I. Figure 4 schematically illustrates the proposed reaction sequence, revealing the mechanism of ozone degradation. The rate

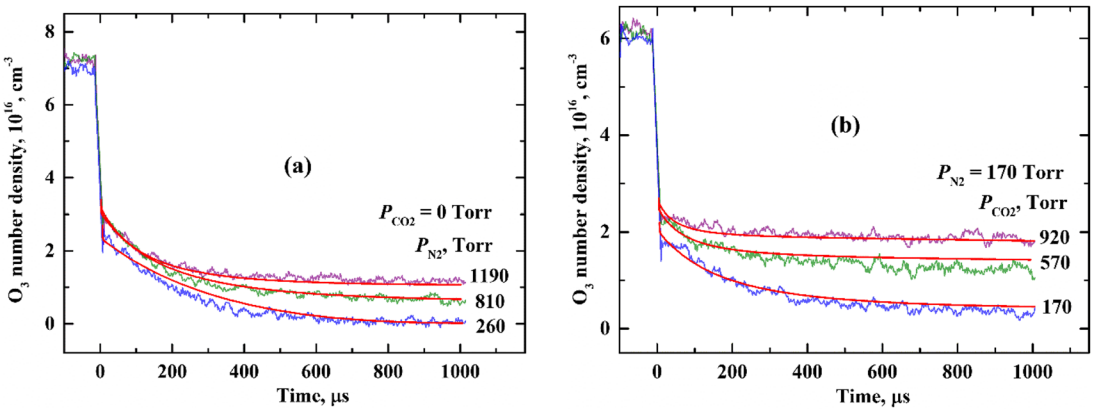

FIG. 3. Temporal profiles of the O_3 number densities (a) at different total pressures of N_2 for the same values of $[O_3]_0 = 2.9 \times 10^{16}$ cm^{-3} and $[O]_0 = 4.2 \times 10^{16}$ cm^{-3} and (b) at different total pressures of CO_2 for the same values of $[O_3]_0 = 2.3 \times 10^{16}$ cm^{-3} and $[O]_0 = 3.8 \times 10^{16}$ cm^{-3}. Smooth curves—profiles calculated using the model proposed in this study.

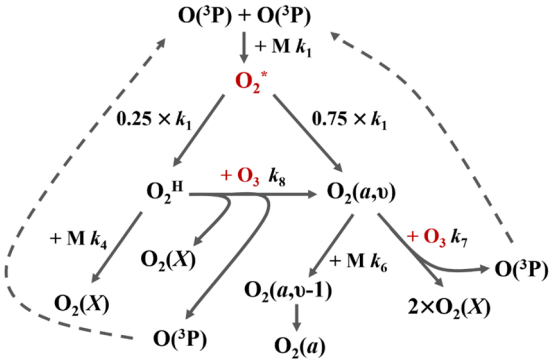

FIG. 4. Reaction sequence scheme revealing the mechanism of ozone degradation due to the recombination of oxygen atoms.

constant for the three-body recombination process 1 for M = N_2 was measured in several studies,[12,19,55,56] and its value is close to 3×10^{-33} cm^6 s^{-1} at T = 300 K.[19] Process 1 with CO_2 is 2.5 times faster than with N_2.[1] The main product of O(^{3}P) ternary association is $O_2(\Pi)$. Its deactivation rates by O_2, N_2, and CO_2 measured using the REMPI method[6] are quite high, and considering that the magnitude of the ratio $[M]/[O_3]_0$ is always close to 3, the hypothetical course of the reaction $O_2(\Pi) + O_3$ can be neglected in our model.

Unlike Krasnopolsky,[1] we combined the three Herzberg states into one "effective state" $O_2{}^H$. The total calculated yield of $O_2{}^H$ in process 1 is 0.25 at T = 300 K,[25,26] and its production is described by process 1a. The product of Π state quenching is the subject of discussions. Krasnopolsky[1] reported that the IR atmospheric band at 1.27 μm in Earth's nightglow and on Venus is excited mostly by the energy transfer in the $O_2(\Pi) + O_2$ and $O_2(\Pi) + CO_2$ quenching processes, respectively. The yields of $O_2(a)$ in these processes vary within 0.8–0.9. Taking into account the rapid deactivation rate of the quintet state, quenching of the b state to a, and neglecting the production of $O_2(X)$, formation of vibrationally excited $O_2(a, \upsilon)$ occurs in our model via process 1b.

Considering the rate constants for processes involving $O_2{}^H$, the choice was made in favor of the known values for the triplet A and A' states because their yields are almost 90% of the total nascent $O_2{}^H$ yield in process 1 and processes involving them should result in the same products despite the difference in their chemical reactivity.[57] In this case, quenching of $O_2{}^H$ by N_2 and CO_2 (process 4) is spin allowed only to the ground state $O_2(X)$,[1] which did not allow us to set the effective yield of singlet oxygen equal to 1. The values of the rate constants for process 4 at M = N_2, available in the literature, are in a wide range from 3×10^{-12} cm^3 s^{-1} (Ref. 1) to 9×10^{-15} cm^3 s^{-1} (Ref. 29). In our model, the rate constant $k_4^{N_2}$ was fixed at 2×10^{-13} cm^3 s^{-1}. At the same time, the rate constant of process 4 at M = CO_2 coincided with the experimentally measured value.[21] In addition, we introduced process 8 with the rate constant close to the gas-kinetic limit. Taking into account the above assumptions, the only adjustable parameters in our model were rate constants k_7 and k_8. In our consideration, rate constant k_8 combines reactions of all three Herzberg states with ozone. It should be noted, however, that the Herzberg $A'^3\Delta_u$ state was shown theoretically to exhibit the highest reactivity toward closed shell molecules among the three states,[57,58] which, in the present case of ozone, can be attributed to the fact that the $O_2(A'^3\Delta_u) + O_3$ reactants are directly correlated with the O(^{3}P) + $O_2(X)$ products in a triplet electronic state [see the correlation diagram in Fig. 5(a)].

Since a large amount of energy is released during the quenching process 1b, high vibrational levels of the $O_2(a)$ molecule become populated. Kinetic data are available for $O_2(a, \upsilon = 1–3)$ quenching,[22,23,46] but those are missing for $\upsilon > 3$. Park and Slanger[59] reported the $O_2(X, \upsilon)$ quenching rate constants with N_2 and CO_2 at T = 300 K. They found that the rate constants increase with the vibrational quantum number in the range of υ = 8–20. It is reasonable to assume that the rate constant for $O_2(a, \upsilon)$ removal by N_2 and CO_2 grows with υ to the same extent as for $O_2(X, \upsilon)$. The differential rate equations for populations of $O_2(a, \upsilon)$ vibrational levels υ are as follows:

$$\frac{d[O_2(a,\upsilon)]}{dt} = [M]\left(f_\upsilon k_{1b}^M [O]^2 - k_{\upsilon\to\upsilon-1}^M [O_2(a,\upsilon)] + k_{\upsilon\to\upsilon-1}^M \exp(-E_\upsilon/RT)[O_2(a,\upsilon-1)] + k_{\upsilon+1\to\upsilon}^M \times [O_2(a,\upsilon+1)] - k_{\upsilon+1\to\upsilon}^M \exp(-E_{\upsilon+1}/RT) \times [O_2(a,\upsilon)]\right) - k_7[O_2(a,\upsilon)][O_3]. \quad \text{(E1)}$$

The differential rate equations for other variable species are

$$\frac{d[O]}{dt} = -2k_1^M[O]^2[M] + [O_3]\left(k_7\sum_{\upsilon>2}[O_2(a,\upsilon\geq 3)] + k_8[O_2{}^H] + k_9\sum_{\upsilon\leq 2}[O_2(a,\upsilon\leq 2)] - k_{10}[O]\right), \quad \text{(E2)}$$

$$\frac{d[O_3]}{dt} = -[O_3]\left(k_7\sum_{\upsilon>2}[O_2(a,\upsilon\geq 3)] + k_8[O_2{}^H] + k_9\sum_{\upsilon\leq 2}[O_2(a,\upsilon\leq 2)] + k_{10}[O]\right), \quad \text{(E3)}$$

$$\frac{d[O_2{}^H]}{dt} = k_{1a}^M[O]^2[M] - [O_2{}^H]\left(k_2[O] + k_3[O_2(a)] + k_4^M[M] + k_8[O_3]\right), \quad \text{(E4)}$$

where $k_{\upsilon\to\upsilon-1}^M$ is the rate constant for process 6 and E_υ is the energy of $O_2(a)$ vibrational level υ. The exponential terms in these equations reflect the rates of the uptake of the vibrational quanta upward. The first term in brackets in equation (E1) describes the population of the υ-th vibrational level of $O_2(a)$ with probability f_υ.

The last term of (E1) describes the loss of $O_2(a, \upsilon)$ and O_3 in process 7. In order to consider possible mechanisms of this process, we carried out some preliminary calculations on the O_5 potential energy surface (PES) in singlet and triplet electronic states. It should be noted that according to experimental enthalpies of formation,[60] the $O_2(X) + O_3 \rightarrow$ O(^{3}P) + $2O_2(X)$ reaction is endothermic by 24.5 kcal/mol, which makes the ground electronic state molecular oxygen unreactive with ozone under ambient conditions. Alternatively, reaction 9 is nearly thermoneutral (+1.8 kcal/mol) but is spin-forbidden since the product consisting of three triplet fragments can overall constitute either triplet or septet spin state—see Fig. 5(a) for the correlation diagram between different electronic states of the

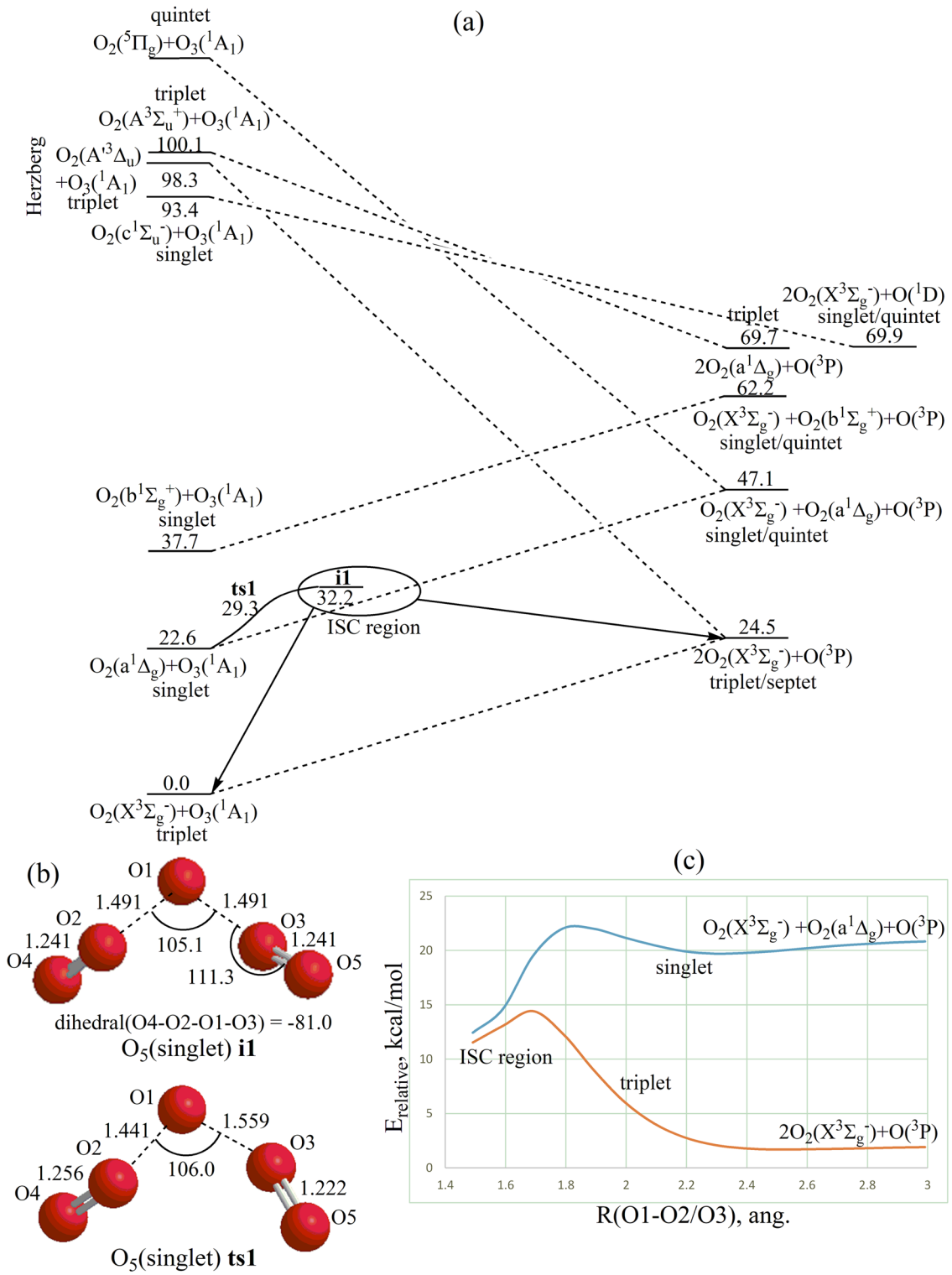

FIG. 5. (a) Correlation diagram between different electronic states of the O_2 + O_3 reactants and O + $2O_2$ products and the supposed position of the singlet–triplet ISC region. The energies of different electronic states are taken from experiment.[60,67] (b) Optimized geometries of O_5 **i1** and **ts1** in the singlet electronic state. (c) Calculated potential energy profiles for the decomposition of **i1** in singlet and triplet electronic states from **i1** to the O + $2O_2$ products within C_2 symmetry along the O1–O2/O3 distance (right panel). All calculations were performed at the UωB97XD/cc-pVTZ level of theory.

reactants $O_2 + O_3$ and products $O + 2O_2$. Therefore, the reaction is likely to proceed via singlet–triplet intersystem crossing. We first looked for local minima on the O_5 singlet PES using the unrestricted UωB97XD density functional method[61] with Dunning's cc-pVTZ basis set[62] using the Gaussian 09 package,[63] allowing the singlet wavefunction to have an open shell biradical character. Geometry optimization converged to a C_2-symmetric O_5 intermediate **i1** (Fig. 5) in which the central O1 atom is weakly bound (1.491 Å) with two O_2 molecules with a slightly elongated O–O bond [1.241 vs 1.208 Å in $O_2(X)$]. A transition state **ts1** for the decomposition of **i1** back to the $O_2(a) + O_3$ reactants was also located [Fig. 5(b)], and its connection with $O_2(a) + O_3$ and **i1** was verified by intrinsic reaction coordinate calculations. In **ts1**, the O1–O3 distance elongates to 1.559 Å, whereas O1–O2 shortens to 1.441 Å. The relative energies of **i1** and **ts1** calculated at the UωB97XD/cc-pVTZ + ZPE level with respect to the $O_2(a) + O_3$ reactants are 12.6 and 12.9 kcal/mol, respectively, thus showing metastability of the complex **i1**. The UωB97XD/cc-pVTZ energies may not be sufficiently accurate; while this level of theory reasonably reproduces the experimental reaction energy of $O_2(a) + O_3 \rightarrow O(^3P) + 2O_2(X)$ (+0.3 kcal/mol), the $O_2(a)$–$O_2(X)$ energy gap is significantly underestimated (11.6 kcal/mol vs experimental 22.6 kcal/mol). Hence, we refined the relative energies of **i1** and **ts1** [with respect to the $O_2(a) + O_3$ supermolecule] using the multireference second-order perturbation theory[64,65] CASPT2(14, 12)/cc-pVTZ approach with the active space including 14 electrons distributed on 12 orbitals, utilizing the MOLPRO 2010 package;[66] the corresponding seven highest occupied and five lowest unoccupied orbitals were chosen for the active space. The CASPT2(14,12)/cc-pVTZ + ZPE(UωB97XD/cc-pVTZ) calculations lower the energies of **i1** and **ts1** to 9.6 and 6.7 kcal/mol, respectively, further emphasizing the metastable character of **i1**. To explore the further fate of this complex in the direction of the $O(^3P) + 2O_2(X)$ products, we scanned both the triplet and singlet PESs at the UωB97XD/cc-pVTZ level beginning from **i1** within C_2 symmetry by eventually elongating the R(O1–O2/O3) distance from ~1.5 to 3 Å. The resulting potential energy profiles are illustrated on the right panel of Fig. 5(c). One can see that the energies of the singlet and triplet states are close in the vicinity of **i1**, with the difference at **i1** being only 0.9 kcal/mol. This result indicates that singlet–triplet intersystem crossing is likely to occur in this region of the PES. While the singlet state energy generally grows when the central O1 atom moves away from the two O_2 fragments, the triplet state energy decreases (overcoming a little bump at ~1.7 Å), reaching the energy of the $O(^3P) + 2O_2(X)$ products in the asymptote. Transition state search in the triplet state starting from the structure corresponding to the maximum on the minimal energy profile curve was unsuccessful, whereas geometry optimization leads to dissociation either to the products or to $O_2(X) + O_3$ depending on small alterations in the initial O1–O2/O3 distance. This shows that triplet **i1** is unstable and, beginning from the intersystem crossing region (ISC), the system in the triplet state may spontaneously decompose to $O(^3P) + 2O_2(X)$ or go back to $O_2(X) + O_3$. Alternatively, the singlet surface converges to the $O(^3P) + O_2(X) + O_2(a)$ products in the asymptote. Thus, the reaction mechanism can be speculated as follows: $O_2(a) + O_3 \rightarrow$ **ts1** $\rightarrow$ **i1** $\rightarrow$ singlet–triplet intersystem crossing $\rightarrow O(^3P) + 2O_2(X)$, and the reaction rate constant would be likely controlled by the energy of the intersystem crossing region (ISC) in the vicinity of **ts1**/**i1** and the probability of the intersystem crossing. According to the CASPT2 results, the energy in this vicinity is 9.6 kcal/mol, which lies between two and three quanta of vibrational excitation of $O_2(a)$ (8.5 and 12.7 kcal/mol, respectively), and hence, the reactions of $O_2(a, v)$ with $v \geq 3$ with O_3 could indeed be fast.

Time dependences of the number densities $[O_2(a, v = 0–20)]$ were determined by solving the system of differential equations (E1). The initial post-photolysis number density of $O_2(a)$ was set to be equal to $[O_2(a)]_0 = 0.9 \times \Delta[O_3]_{ph}$. Thus, its initial distribution over vibrational levels $v = 0$, 1, 2, and 3 was fixed at $0.57 \times [O_2(a)]_0$, $0.24 \times [O_2(a)]_0$, $0.12 \times [O_2(a)]_0$, and $0.07 \times [O_2(a)]_0$, respectively. The initial number densities of $O_2(a, v)$ with $v = 4–20$ and O_2^H were set to zero $[O_2(a, v = 4–20)]_0 = [O_2^H]_0 = 0$. The initial values for the oxygen atom and ozone molecule were $[O]_0 = \Delta[O_3]_{ph}$ and $[O_3]_0 = [O_3]_{in} - \Delta[O_3]_{ph}$ (see Fig. 1). The rate constants for processes 7 and 8 are unknown. In the model, they were treated as variable parameters. The analysis of the experimental data using the proposed kinetic model is complicated by the lack of any information on the dependence of the rate constant for process 6 on the vibrational quantum number v and nascent vibrational level distribution of $O_2(a, v)$ in the secondary processes.

To find how the values of k_6 and f_v affect the result, calculations were carried out with several options:

Case I—$k_6(v) = v \times k^M_{1\rightarrow0}$; $f_v = 0.1$ through $v = 6–15$;
Case II—$k_6(v) = v \times k^M_{1\rightarrow0}$; $f_v = 0.0555$ through $v = 1–18$;
Case III—$k_6(v) = v \times k^M_{1\rightarrow0}$; f_v is an equilateral triangle with base $v = 1–18$;
Case IV—$k_6(v) = 3 \times k^M_{1\rightarrow0}$; f_v is an equilateral triangle with base $v = 1–18$; and
Case V—$k_6(v) = v \times k^M_{1\rightarrow0}$; f_v is an equilateral triangle with base $v = 3–18$.

Figure 6 illustrates the distributions of f_v over vibrational levels for cases I–V. The red solid curves in Figs. 1–3 show the calculated temporal profiles of O_3 number densities for case I. The most satisfactory fit to the entire dataset was obtained using the rate constants $k_7 = (3 \pm 1) \times 10^{-11}$ cm^3 s^{-1} and $k_8 = (2 \pm 1) \times 10^{-10}$ cm^3 s^{-1}. The presented errors in the rate constants cover the entire range of values assumed for k_7 and k_8 during the fitting. Taking into account that the

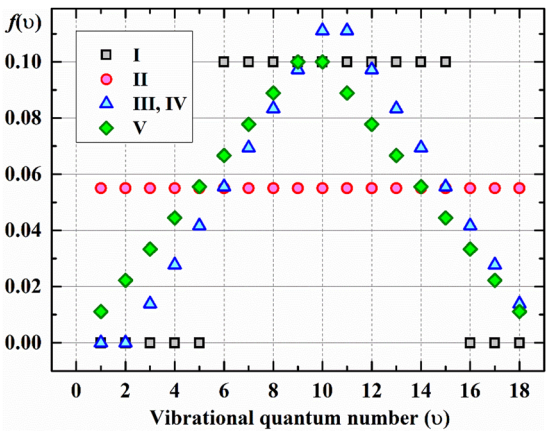

FIG. 6. Distributions of f_v over vibrational levels for cases I–V.

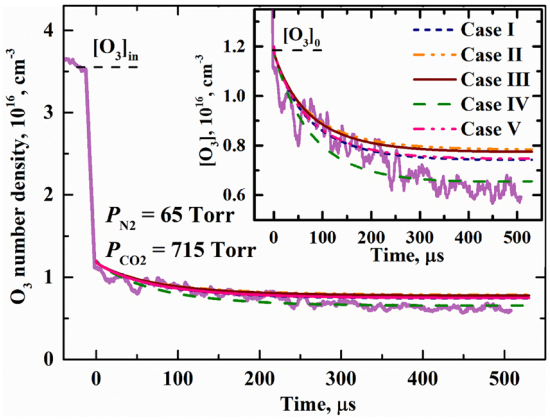

FIG. 7. The upper $[O_3]$ temporal profile from Fig. 1. Signal in the inset shows the enlarged section of the profile. Curves illustrate the modeling results for the five considered cases.

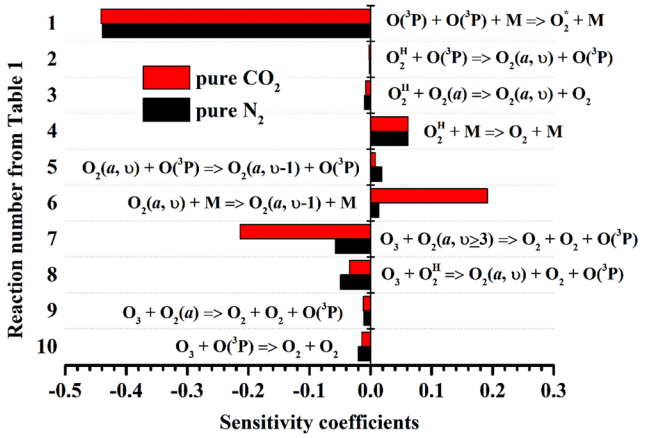

FIG. 8. Sensitivity analysis for the ozone number density in pure N_2 (black columns) and CO_2 (red columns) under the initial conditions from Fig. 1.

excitation energy of $O_2(a, v \geq 3)$ is only sufficient to overcome the energy barrier of reaction 7, as shown above, loss of ozone in the reactions with $O_2(a, v = 1$ and $2)$ was neglected.

Figure 7 exhibits the calculated temporal profiles of the ozone number density for P_{CO_2} = 715 Torr and P_{N_2} = 65 Torr. Results of the calculations showed weak dependence on the choice of $k_6(v)$ and f_v because of high rates of processes 7 and 8. For experiments with pure N_2, the difference between the cases I–V was almost indistinguishable due to the fact that the rate of reactive process 7 under our experimental conditions was always much higher than that for relaxation process 6 with N_2. The rate ratio

$$\frac{k_7[O_3]}{k_6^{N_2}[N_2] + k_6^{CO_2}[CO_2]}$$

decreases when replacing CO_2 by N_2, and as a consequence, the calculated $[O_3]$ profiles for all cases converge closer and closer with an increase in the degree of dilution with nitrogen.

In order to clarify the main reactions affecting ozone number density, sensitivity analysis was carried out in cases of pure N_2 and CO_2. The results of the analysis are shown in Fig. 8. As shown, the main reactions responsible for changing the O_3 number density are 1, 6, 7, and 8. The reaction sensitivity of process 1 is the highest both in pure N_2 and CO_2 by a wide margin with respect to the other reactions. This is due to that process 1 produces both components responsible for the rapid destruction of O_3 and thus directly limits the rates of reactions 7 and 8. The sensitivities of processes 7 and 8 for the case of pure nitrogen are approximately the same, and their values are 8 times lower than that for process 1. However, the sensitivity coefficient of process 7 in pure CO_2 is four times larger than in N_2. In addition, the sensitivity coefficients of processes 6 and 7 are practically equal in the magnitude. This means that processes 6 and 7 compete with one another because the rate constant of quenching of $O_2(a, v)$ by CO_2 is two orders of magnitude higher than by N_2. At the same time, process 6 only slightly suppresses reaction 7 in

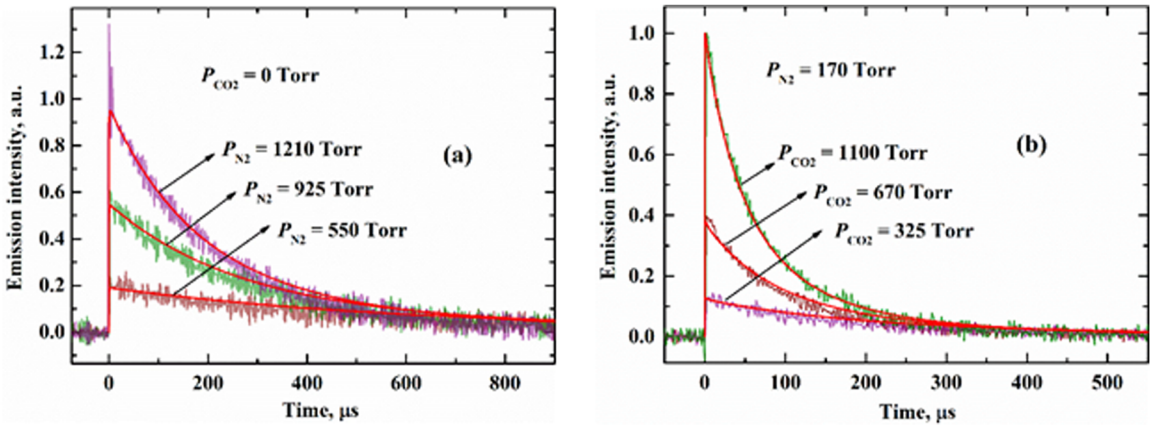

FIG. 9. Emission signals near 567 nm at $[O]_0 = 2.6 \times 10^{16}$ cm^{-3} and $[O_3]_0 = 2.9 \times 10^{16}$ cm^{-3} for three different pressures of N_2 (a) and CO_2 (b). Smooth curves represent temporal profiles of $[O_2^H]$ calculated using the model proposed in this study.

the case of pure nitrogen. Thus, all sensitivity analysis results are in complete agreement with the experimental observations.

The proposed kinetic mechanism was applied to reproduce the emission intensities from Herzberg states. The emission spectrum of the post-photolysis glow in the N_2/O_3 mixture was obtained at the total pressure of 1 atm in the range 550–650 nm. Two distinct peaks were observed near 567 and 615 nm, corresponding to weak emission transitions $O_2(c, v = 0) \rightarrow O_2(a, v = 5)$ and $O_2(c, v = 0) \rightarrow O_2(a, v = 6)$, respectively.[68] Emission signals in the region of 567 nm obtained at different total pressures of N_2 and CO_2 and initial number densities $[O]_0 = 2.6 \times 10^{16}$ cm^{-3} and $[O_3]_0 = 2.9 \times 10^{16}$ cm^{-3} are presented in Fig. 9. Evidently, both the production and decay rates of the c state grow with pressure of the buffer gas M. Experimental data presented in Figs. 1–3 and 9 indicate that time scales for $[O_3]$ and $\left[O_2^H\right]$ decays are of the same order of magnitude. Calculated temporal profiles of $[O_2^H]$ (smooth curves in Fig. 9) are in excellent agreement with the detected signals.

IV. CONCLUSIONS

Thus, the experimental data presented in this work clearly show that recombination of oxygen atoms obtained by UV photolysis of ozone is accompanied by a rapid loss of O_3 molecules. The time scale for ozone removal is of the same order of magnitude as for O_2^H loss. The kinetic model developed for the oxygen nightglow on the terrestrial planets[1] and adopted for the laboratory photolysis experiments adequately describes the detected temporal profiles of the ozone number density and O_2^* emission intensities.

According to our model, the main channel of ozone destruction is the chemical reaction between O_3 and vibrationally excited singlet oxygen $O_2(a, v \geq 3)$. There are two paths of $O_2(a, v \geq 3)$ production listed in Table I. The first one is a collisional relaxation of the quintet state Π described above. The second one is the $O_3 + O_2^H$ reaction, which, according to our assumption, yields $O_2(a, v \geq 3)$ (process 8). This assumption is based on the fact that under certain conditions, we observed the loss of more than one ozone molecule caused by one O_2^* molecule.

Seven electronic states of molecular oxygen are involved in the kinetics of the post-photolysis mixture O_3/M. The situation is complicated by the fact that on the course of secondary energy exchange processes, a large number of vibrational levels of each of the electronic states are populated. Kinetic constants are known only for a small fraction of the whole variety of elementary energy exchange processes in this system. The simplified kinetics presented in Table I contains a number of assumptions and cannot claim high accuracy in reproducing experimental data. Therefore, the deduced values of the rate constants for processes 7 and 8, $k_7 = 3 \times 10^{-11}$ cm^3 s^{-1} and $k_8 = 2 \times 10^{-10}$ cm^3 s^{-1}, should be considered as estimates.

Ab initio calculations allowed us to propose a reaction pathway from the reactants to products on the O_5 potential energy surface. The calculations revealed that the $O_2(a) + O_3$ reaction is likely to proceed via singlet–triplet intersystem crossing exhibiting an energy barrier of 9.6 kcal/mol, which lies between two and three quanta of vibrational excitation of $O_2(a)$, and hence, $O_2(a, v)$ with $v \geq 3$ could rapidly react with ozone. It should be noted that the present theoretical consideration regarding process 7 is of a qualitative character, whereas a more quantitative characterization of the O_5 PES can be achieved through multireference geometry optimization (e.g., CASSCF) of **ts1**, **i1**, and the intersystem crossing and the energy refinement at the CASPT2 level with carefully selected active spaces. This could be done in the future but is beyond the scope of the present work.

The rates of the recombination processes 1 and $O(^3P) + O_2 + M \rightarrow O_3 + M$ (reaction 11) are comparable at altitudes of Earth's atmosphere of about 100 km.[34] Reactions 7 and 8 may contribute to a loss of O_3 molecules formed in the three-body recombination process 11 but are not included into current photochemical models of the upper atmosphere. Hence, the results of the present study indicate how the current models can be improved.

ACKNOWLEDGMENTS

The experimental studies at Lebedev Physical Institute were supported by the Ministry of Science and Higher Education of the Russian Federation by Contract No. 075-15-2021-597. The kinetic modeling at Samara University was supported by RFBR Grant No. 19-33-90265.

AUTHOR DECLARATIONS

Conflict of Interest

The authors have no conflicts to declare.

DATA AVAILABILITY

The data that support the findings of this study are available from the corresponding author upon reasonable request.

REFERENCES

[1] V. A. Krasnopolsky, Planet. Space Sci. **59**, 754 (2011).
[2] V. A. Krasnopolsky, A. A. Krysko, V. N. Rogachev, and V. A. Parshev, Cosm. Res. **14**, 789 (1976).
[3] T. J. Fauchez, G. L. Villanueva, E. W. Schwieterman, M. Turbet, G. Arney, D. Pidhorodetska, R. K. Kopparapu, A. Mandell, and S. D. Domagal-Goldman, Nat. Astron. **4**, 372 (2020).
[4] E. W. Schwieterman, V. S. Meadows, S. D. Domagal-Goldman, D. Deming, G. N. Arney, R. Luger, C. E. Harman, A. Misra, and R. Barnes, Astrophys. J. **819**, L13 (2016).
[5] L. Ben-Jaffel and G. E. Ballester, Astron. Astrophys. **553**, A52 (2013).
[6] T. G. Slanger and R. A. Copeland, Chem. Rev. **103**, 4731 (2003).
[7] D. L. Huestis, Geophys. Monogr. Ser. **130**, 245–259 (2002).
[8] R. J. A. Scheidsbach and D. H. Parker, Phys. Chem. Chem. Phys. **21**, 14278 (2019).
[9] A. S. Kirillov and V. B. Belakhovsky, J. Geophys. Res.: Atmos. **126**, e2020JD033177, https://doi.org/10.1029/2020jd033177 (2021).
[10] K. S. Kalogerakis, Sci. Adv. **5**, eaau9255 (2019).
[11] V. Yankovsky, Adv. Space Res. **67**, 921 (2021).
[12] D. A. Pejaković, K. S. Kalogerakis, R. A. Copeland, and D. L. Huestis, J. Geophys. Res.: Space Phys. **113**, 4303, https://doi.org/10.1029/2007ja012694 (2008).
[13] M. Grygalashvyly and G. R. Sonnemann, Earth, Planets Space **72**, 187 (2020).
[14] B. F. Minaev and A. A. Panchenko, J. Phys. Chem. A **124**, 9638 (2020).
[15] D. R. Bates, Planet. Space Sci. **27**, 717 (1979).
[16] V. Yankovsky and E. Vorobeva, Atmosphere **11**, 116 (2020).
[17] M. Grygalashvyly, B. Strelnikov, M. Eberhart, J. Hedin, M. Khaplanov, J. Gumbel, M. Rapp, F.-J. Lübken, S. Löhle, and S. Fasoulas, J. Atmos. Sol.-Terr. Phys. **213**, 105522 (2021).
[18] O. Lednyts'kyy and C. Von Savigny, Atmos. Chem. Phys. **20**, 2221 (2020).
[19] G. P. Smith and R. Robertson, Chem. Phys. Lett. **458**, 6 (2008).

[20]R. D. Kenner and E. A. Ogryzlo, Can. J. Phys. **62**, 1599 (1984).
[21]R. D. Kenner and E. A. Ogryzlo, Can. J. Chem. **61**, 921 (1983).
[22]D. A. Pejaković, Z. Campbell, K. S. Kalogerakis, R. A. Copeland, and T. G. Slanger, J. Chem. Phys. **135**, 094309 (2011).
[23]A. P. Torbin, A. A. Pershin, A. M. Mebel, M. V. Zagidullin, M. C. Heaven, and V. N. Azyazov, Chem. Phys. Lett. **691**, 456 (2018).
[24]International Union of Pure and Applied Chemistry (IUPAC), Evaluated Kinetic Data. available at https://iupac-aeris.ipsl.fr/.
[25]P. C. Wraight, Planet. Space Sci. **30**, 251 (1982).
[26]I. W. M. Smith, Int. J. Chem. Kinet. **16**, 423 (1984).
[27]K. Knutsen, M. J. Dyer, and R. A. Copeland, J. Chem. Phys. **101**, 7415 (1994).
[28]E. S. Hwang and R. A. Copeland, Geophys. Res. Lett. **24**, 643, https://doi.org/10.1029/97gl00547 (1997).
[29]R. D. Kenner and E. A. Ogryzlo, Chem. Phys. Lett. **103**, 209 (1983).
[30]J. Wildt, G. Bednarek, E. H. Fink, and R. P. Wayne, Chem. Phys. **156**, 497 (1991).
[31]R. A. Copeland, K. Knutsen, M. E. Onishi, and T. Yalçin, J. Chem. Phys. **105**, 10349 (1996).
[32]A. S. Kirillov, Chem. Phys. Lett. **592**, 103 (2014).
[33]K. S. Kalogerakis, A. Totth, P. C. Cosby, T. G. Slanger, and R. A. Copeland, EOS, Trans. AGU **81**, F944 (2000).
[34]V. N. Azyazov and M. C. Heaven, Int. J. Chem. Kinet. **47**, 93 (2015).
[35]A. V. Volynets, D. V. Lopaev, T. V. Rakhimova, O. V. Proshina, A. A. Chukalovsky, and J. P. Booth, Plasma Sources Sci. Technol. **29**, 115020 (2020).
[36]L. D. Pietanza, G. Colonna, and M. Capitelli, Phys. Plasmas **27**, 093510 (2020).
[37]A. V. Pelevkin and A. S. Sharipov, Plasma Chem. Plasma Process. **39**, 1533 (2019).
[38]S. Y. Pichugin and M. C. Heaven, Chem. Phys. **425**, 80 (2013).
[39]F. An, J. Chen, X. Hu, H. Guo, and D. Xie, J. Phys. Chem. Lett. **11**, 4768 (2020).
[40]M. V. Zagidullin, N. A. Khvatov, I. A. Medvedkov, G. I. Tolstov, A. M. Mebel, M. C. Heaven, and V. N. Azyazov, J. Phys. Chem. A **121**, 7343 (2017).
[41]N. A. Khvatov, M. V. Zagidullin, G. I. Tolstov, I. A. Medvedkov, A. M. Mebel, M. C. Heaven, and V. N. Azyazov, Chem. Phys. **521**, 85 (2019).
[42]M. B. Knickelbein, K. L. Marsh, O. E. Ulrich, and G. E. Busch, J. Chem. Phys. **87**, 2392 (1987).
[43]K. S. Kalogerakis, R. A. Copeland, and T. G. Slanger, J. Chem. Phys. **116**, 4877 (2002).
[44]D. A. Pejaković, R. A. Copeland, T. G. Slanger, and K. S. Kalogerakis, Chem. Phys. Lett. **403**, 372 (2005).
[45]D. A. Pejaković, E. R. Wouters, K. E. Phillips, T. G. Slanger, R. A. Copeland, and K. S. Kalogerakis, J. Geophys. Res. **110**, A03308, https://doi.org/10.1029/2004JA010860 (2005).
[46]T. G. Slanger, E. S. Hwang, N. C.-M. Bartlett, and K. S. Kalogerakis, J. Phys. Chem. A **122**, 8114 (2018).
[47]A. S. Kirillov, Quantum Electron. **42**, 653 (2012).
[48]A. S. Kirillov, Chem. Phys. **410**, 103 (2013).
[49]J. Shi and J. R. Barker, J. Geophys. Res. **97**, 13039, https://doi.org/10.1029/92jd00571 (1992).
[50]T. G. Slanger and R. A. Copeland, SRI Project PYU 1205, Contract No. NAG2-1022, MP 97-034, 1997.
[51]M. J. Kurylo, W. Braun, A. Kaldor, S. M. Freund, and R. P. Wayne, J. Photochem. **3**, 71 (1974).
[52]R. K. Sparks, L. R. Carlson, K. Shobatake, M. L. Kowalczyk, and Y. T. Lee, J. Chem. Phys. **72**, 1401 (1980).
[53]A. A. Pershin, A. P. Torbin, M. C. Heaven, and V. N. Azyazov, Bull. Lebedev Phys. Inst. **43**, 20 (2016).
[54]J. Tellinghuisen and L. F. Phillips, J. Phys. Chem. **90**, 5108 (1986).
[55]I. M. Campbell and C. N. Gray, Chem. Phys. Lett. **18**, 607 (1973).
[56]J. E. Morgan and H. I. Schiff, J. Chem. Phys. **38**, 1495 (1963).
[57]B. F. Minaev and G. I. Kobzev, Spectrochim. Acta, Part A **59**, 3387 (2003).
[58]B. F. Minaev, S. Lunell, and G. I. Kobzev, Int. J. Quantum Chem. **50**, 279 (1994).
[59]H. Park and T. G. Slanger, J. Chem. Phys. **100**, 287 (1994).
[60]B. Ruscic and D. H. Bross, Active Thermochemical Tables (ATcT) values based on ver. 1.122p of the Thermochemical Network (2020); available at https://ATcT.anl.gov.
[61]J.-D. Chai and M. Head-Gordon, Phys. Chem. Chem. Phys. **10**, 6615 (2008).
[62]T. H. Dunning, J. Chem. Phys. **90**, 1007 (1989).
[63]M. J. Frisch, G. W. Trucks, H. B. Schlegel, G. E. Scuseria, M. A. Robb, J. R. Cheeseman, G. Scalmani, V. Barone, B. Mennucci, G. A. Petersson, H. Nakatsuji, M. Caricato, X. Li, H. P. Hratchian, A. F. Izmaylov, J. Bloino, G. Zheng, L. Sonnenberg, M. Hada, M. Ehara, K. Toyota, R. Fukuda, J. Hasegawa, M. Ishida, T. Nakajima, Y. Honda, H. Nakai, T. Vreven, J. A. Montgomery, J. E. Peralta, F. Ogliaro, M. Bearpark, J. J. Heyd, E. Brothers, K. N. Kudin, V. N. Staroverov, T. Keith, R. Kobayashi, J. Normand, K. Raghavachari, A. Rendell, J. C. Burant, S. S. Iyengar, J. Tomasi, M. Cossi, N. Rega, J. M. Millam, M. Klene, J. E. Knox, J. B. Cross, V. Bakken, C. Adamo, J. Jaramillo, R. Gomperts, R. E. Stratmann, O. Yazyev, A. J. Austin, R. Cammi, C. Pomelli, J. W. Ochterski, R. L. Martin, K. Morokuma, V. G. Zakrzewski, G. A. Voth, P. Salvador, J. J. Dannenberg, S. Dapprich, A. D. Daniels, O. Farkas, J. B. Foresman, J. V. Ortiz, J. Cioslowski, and D. J. Fox, Gaussian 09, 2010.
[64]H.-J. Werner, Mol. Phys. **89**, 645 (1996).
[65]P. Celani and H.-J. Werner, J. Chem. Phys. **112**, 5546 (2000).
[66]H.-J. Werner, P. J. Knowles, G. Knizia, F. R. Manby, and M. Schütz, Wiley Interdiscip. Rev.: Comput. Mol. Sci. **2**, 242 (2012).
[67]S. G. Lias, J. E. Bartmess, J. F. Liebman, J. L. Holmes, R. D. Levin, and W. G. Mallard, Natl. Inst. Stand. Technol. Gaithersbg. MD **20899**, (2018).
[68]T. G. Slanger, J. Chem. Phys. **69**, 4779 (1978).